Invited Paper

Terahertz and Ultrafast Dynamics of Carriers and Phonons in Graphene and Carbon Nanotubes

Weilu Gao[a], Qi Zhang[a], Lei Ren[a], Zehua Jin[a], Ji-Hee Kim[b], and Junichiro Kono[a,c]

[a]Department of Electrical and Computer Engineering, Rice University, Houston, Texas, U.S.A.;
[b]Center for Integrated Nanostructure Physics (CINAP), Institute for Basic Science (IBS), Sungkyunkwan University, Suwon, Republic of Korea;
[c]Department of Physics and Astronomy and Department of Materials Science and NanoEngineering, Rice University, Houston, Texas, U.S.A.

ABSTRACT

Graphene and carbon nanotubes provide a variety of new opportunities for fundamental and applied research. Here, we describe results of our recent terahertz and ultrafast studies of carriers and phonons in these materials. Time-domain terahertz spectroscopy is a powerful method for determining the basic properties of charge carriers in a non-contact manner. We show how one can modulate the transmission of terahertz waves through graphene by gating and how one can improve the modulation performance by combining graphene with apertures and gratings. In carbon nanotubes, we demonstrate that the terahertz response is dominated by plasmon oscillations, which are enhanced by collective antenna effects when the nanotubes are aligned. Finally, ultrafast spectroscopy of carbon nanotubes allow us to excite and probe coherent phonons, both in the low-energy radial breathing mode and high-energy G-mode, which are strongly coupled with excitonic interband transitions.

Keywords: Carbon nanotubes, graphene, terahertz, ultrafast dynamics

1. INTRODUCTION

Carbon-based nanomaterials — single-wall carbon nanotubes (SWCNTs) and graphene, in particular — attract much attention due to their wide range of novel electronic, photonic, and mechanical properties.[1–4] In particular, they have ideal properties for the development of optoelectronic devices that operate in the mid-infrared (MIR) and terahertz (THz) ranges, including polarizers, modulators, detectors, and sources. They have been predicted, and partially demonstrated, to have superior performance over existing devices.[5] There have been a number of basic optical studies on these materials during the past decade, but most of them were performed in the weak-excitation, quasi-equilibrium regime. In order to probe and assess their performance characteristics as optoelectronic materials under device-operating conditions, it is crucial to strongly drive them and examine their optical properties in highly nonequilibrium conditions.[6]

In this article, we summarize results of a series of experimental studies of the THz and ultrafast dynamics of carriers and phonons performed on graphene[7–9] and SWCNTs.[10–13] We use time-domain THz spectroscopy to probe frequency-dependent conductivities and determine the density and scattering time of charge carriers. Gate-tunable Fermi energies in graphene can be utilized to effectively modulate the transmission of THz waves.[7] When graphene is placed on a grating, normal incidence THz radiation can excite a propagating surface plasmon polariton,[8] which can be used as a notch filter. We show that the modulation contrast ratio can be significantly enhanced by placing a metallic aperture on top of graphene due to the effect of the extraordinary optical transmission.[9] Free carrier absorption in metallic and doped semiconducting SWCNTs takes the form of plasmon resonance, which can be excited when the incident THz wave is linearly polarized along the nanotube axis. The plasmonic nature has been clearly demonstrated in type-separated SWCNT samples,[11] and the effect can be collectively enhanced when a macroscopic number of SWCNTs are aligned.[10] Finally, ultrafast spectroscopy allows us to make time-dependent observations of lattice vibrations.[12,14,15] Using femtosecond pump-probe spectroscopy, we observed coherent phonons (CPs) corresponding to the low-frequency radial breathing mode

Further author information: (Send correspondence to J.K.): E-mail: kono@rice.edu

Ultrafast Phenomena and Nanophotonics XVIII, edited by Markus Betz, Abdulhakem Y. Elezzabi, Jin-Joo Song, Kong-Thon Tsen, Proc. of SPIE Vol. 8984, 89840K · © 2014 SPIE
CCC code: 0277-786X/14/$18 · doi: 10.1117/12.2038295

(RBM) and the high-frequency G-mode. CP signals are resonantly enhanced when the pump pulse resonantly excites excitons, allowing us to obtain precise information on chiralities present in a given SWCNT ensemble. Furthermore, because the bandgap and diameter in SWCNTs are inversely proportional to each other, the bandgap coherently oscillates as the lattice undergoes coherent RBM oscillations,[14] resulting in modulation of interband optical absorption at THz frequencies.

2. TERAHERTZ SPECTROSCOPY OF GATED LARGE-AREA GRAPHENE

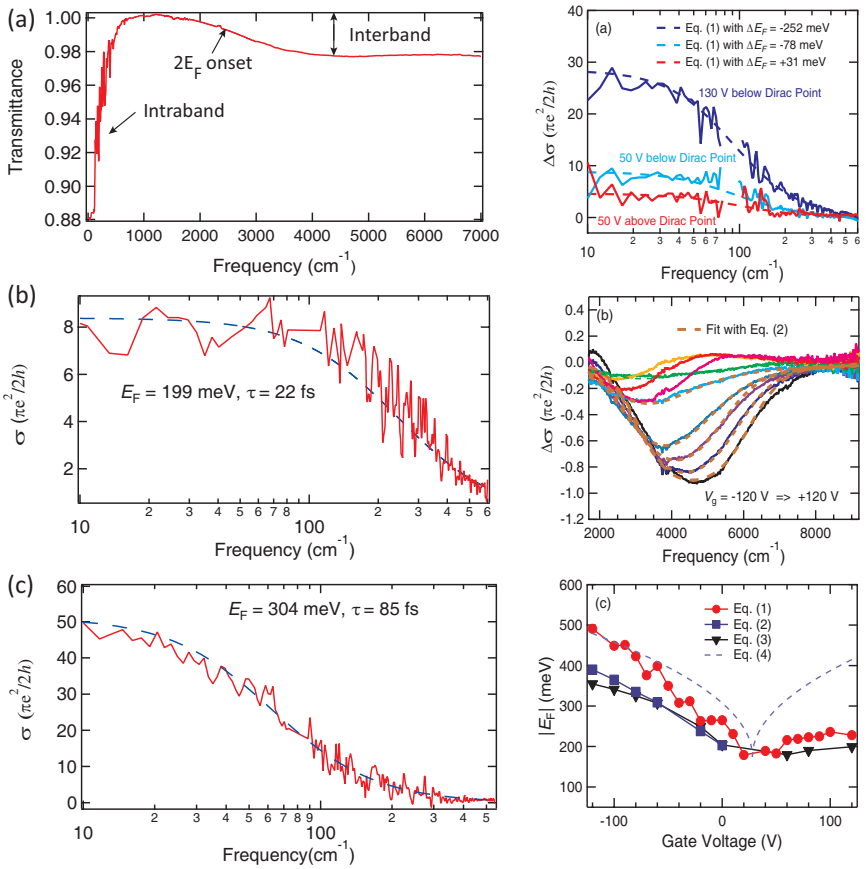

Figure 1. **[LEFT]** (a) Transmittance spectrum of single-layer graphene showing intraband and interband absorption with the "$2E_F$ onset" for interband absorption in between. (b) and (c): Dynamic conductivity of two samples with different Fermi energies and scattering times. **[RIGHT]**[7] Gate-induced dynamic conductivity change of a graphene sample in the THz/MIR frequency range. Gate-induced sheet conductance change for (a) intraband conductivity spectra in the THz region and (b) interband conductivity spectra near the $2E_F$ onset. (c) The gate-induced change of the Fermi level absolute value $|E_F|$ extracted from calculation using Eqs. (1)-(4).

Understanding the ac dynamics of Dirac fermions in graphene is crucial for developing graphene-based THz optoelectronics. Electron-electron interactions and disorder, combined with the unique linear electronic band dispersions, have strong influence on the graphene dynamic conductivity. Furthermore, by analyzing frequency-dependent conductivities one can precisely determine the Fermi energy (E_F) and carrier scattering time (τ). We used a large-area ($\sim$cm^2) field-effect transistor, consisting of single-layer graphene on a SiO_2/p-Si substrate. With applied voltage between the graphene layer and silicon substrate, the transmitted intensity of THz and MIR waves was observed to change with the gate voltage.

A typical transmittance spectrum is shown in Fig. 1[LEFT](a), which exhibits strongly frequency-dependent intraband absorption in the THz and frequency-independent (universal) interband absorption in the mid-infrared

(MIR). Using the standard conducting thin film analysis, the 2D THz conductance spectra can be deduced, as shown in Fig. 1[LEFT](b) and (c) for two different samples with different values of E_F and τ.

Gate-induced change in conductance (compared to the value when $E_F \sim 0$) in the THz range is plotted in Fig. 1[RIGHT](a). Here, the experimental $\Delta\sigma(\omega, V_g) = \sigma(\omega, V_g) - \sigma(\omega, V_0)$ spectra are fit with[16]

$$\sigma_{\text{intra}}(\omega, V_g) = \frac{2ie^2 k_B T}{\pi\hbar^2(\omega + i\gamma)} \ln(e^{E_F(V_g)/k_B T} + e^{-E_F(V_g)/k_B T}), \tag{1}$$

where V_g is the gate voltage, V_0 is the gate voltage at which $E_F \sim 0$ (Dirac point), k_B is the Boltzmann constant, T is the temperature, and $\gamma = \tau^{-1}$. When a gate voltage is applied, the Fermi level moves away from the Dirac point and the overall conductance increases [Fig. 1[RIGHT](a)]. At the same time, E_F can be extracted from the MIR portion of the spectra where the "$2E_F$" onset sensitively changes with V_g,[17,18] as shown in Fig. 1[RIGHT](b). Each MIR spectrum is fit with[16]

$$\sigma_{\text{intra}}(\omega, V_g) = -\frac{ie^2 k_B T}{2\pi\hbar} \int_0^\infty \frac{\sinh(x)}{\cosh[\frac{E_F(V_g)}{k_B T}] + \cosh(x)} \times \frac{\frac{\hbar(\omega+i\Gamma)}{2k_B T}}{x^2 - [\frac{\hbar(\omega+i\Gamma)}{2k_B T}]^2} dx, \tag{2}$$

as presented by the dashed lines, where Γ is the interband transition broadening factor. Another independent method to determine E_F from the MIR spectra is to use the fact that[17,18]

$$\int \Delta\sigma_{\text{inter}}(\omega, V_g) d(\hbar\omega) = 2E_F(V_g)\sigma_0. \tag{3}$$

Figure 1[RIGHT](c) summarizes the gate dependence of E_F obtained through different methods: Eqs. (1)-(4), where (4) is based on a simple capacitor model[19]

$$|E_F(V_g)| = \hbar v_F \sqrt{\pi|\alpha_0(V_g - V_0)|} \tag{4}$$

where $v_F = 1 \times 10^6$ m/s is the Fermi velocity of Dirac fermions in graphene, $\alpha_0 \approx 7 \times 10^{10}$ cm^{-2}V^{-1} and V_0 = 30 V for our case. As shown in Fig. 1[RIGHT](c), there is overall agreement among the four methods, with a strong asymmetry between hole and electron response, which could be due to the induced carriers of silicon near the silicon oxide surface or some trapped charges in the oxide layer.

3. EXCITATION AND ACTIVE CONTROL OF PROPAGATING SURFACE PLASMON POLARITONS IN GRAPHENE

Existing active plasmonic devices based on metals have either slow speeds or limited tunability, while those based on semiconductor 2D electron gases typically work at cryogenic temperatures. In contrast, graphene has been shown to support surface plasmon polaritons (SPPs) with stronger mode confinement and lower propagation loss owing to its unique electronic properties, mainly the high carrier mobility at room temperature. Furthermore, the carrier density in graphene can be electrically tuned efficiently with a small bias voltage, and this unique combination makes graphene a promising platform to build highly integrated active plasmonic devices. To efficiently excite SPPs in graphene with an incident electromagnetic wave, the key challenge is the large wavevector mismatch between the two waves. Optical gratings are widely used to compensate wavevector mismatches, and here we use a silicon grating to excite the SPPs through the guided-wave resonance (GWR).[20] Moreover, the silicon grating can also act as a gate electrode to tune the carrier density in graphene, and thus the resonance frequency varies over a broad range [Fig. 2(a)]. By satisfying the phase matching condition using gratings, the normal-incidence wave will excite SPPs in graphene, and optical energy is dissipated due to the Ohmic loss during the propagation in the graphene layer. Therefore, a notch in transmission is expected around resonance frequency,[21]

$$\omega_0 = \sqrt{\frac{2e^2 E_F}{\hbar^2 \varepsilon_0(\varepsilon_{r1} + \varepsilon_{r2})\Lambda}}, \tag{5}$$

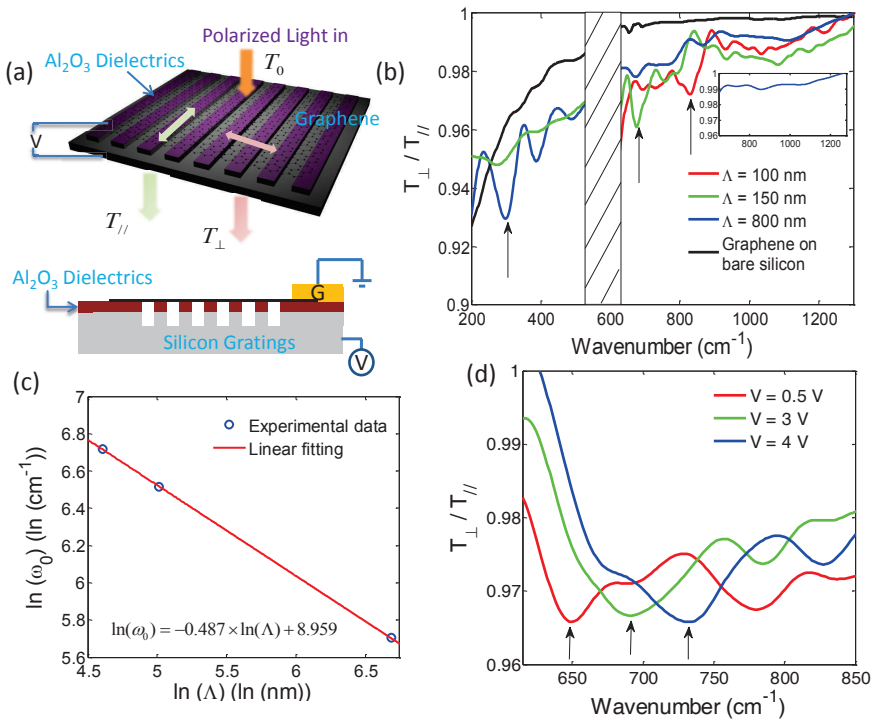

Figure 2. Polarized transmission measurements of graphene plasmonic devices. (a) Schematics of the normal-incidence transmission measurement of silicon-diffractive grating-assisted graphene plasmon excitation by guided-wave resonance (GWR) with two polarizations ($T_\perp$ and $T_\parallel$). (b) Transmission spectra in the THz (200-550 cm^{-1}) and MIR (620-1300 cm^{-1}) for different grating periods. The resonance dips are marked by arrows. The black line is the transmittance of monolayer graphene. The shaded area represents the frequency region where the signal-to-noise ratio was too low. Inset: The transmission spectrum of grating period $\Lambda = 800$ nm in the MIR without graphene. (c) The logarithm of resonance frequency ω_0 versus the logarithm of grating period Λ. A linear fitting with a fitted slope of ~0.487 agrees well with the theoretical prediction of ~0.5 slope in Eq. (5). (d) Electrical tuning of the fabricated GWR graphene plasmonic device with period $\Lambda = 100$ nm. The resonance dips are marked by arrows. Adapted from Ref.[8]

where E_F is the Fermi energy, ε_{r1} and ε_{r2} are the dielectric constants of the materials above and below the graphene film, and Λ is the grating period.

We etched periodically spaced trenches of gratings in a lightly doped silicon substrate with electron beam lithography with various grating periods (Λ). The length and depth of each trench were ~60 μm and ~250 nm, respectively. A 30-nm-thick layer of aluminum oxide was then deposited on top of the grating as the back-gating dielectric layer followed by transferring CVD-grown monolayer graphene onto the grating. Polarization-dependent transmission spectra were taken, as illustrated in Fig. 2(a). Figure 2(b) shows the ratio $T_\perp/T_\parallel$ spectra, indicating a pronounced resonant dip as the incident wave with the correct polarization couples to the graphene SPPs, which scales with the grating period. In contrast, for graphene on a bare silicon wafer, transmission of parallel and perpendicular polarized beams shows no observable resonant features. Figure 2(c) shows the relationship between the logarithm of ω_0 and the logarithm of the grating period Λ, which fits well with Eq. (5). Furthermore, the gate voltage was varied to tune the plasmon resonance, as presented in Fig. 2(d).

4. HIGH-CONTRAST TERAHERTZ WAVE MODULATION BY GATED GRAPHENE ENHANCED BY EXTRAORDINARY OPTICAL TRANSMISSION

Electrically-controllable intraband absorption of graphene makes it a promising platform for building graphene-based active THz devices. Compared with previous THz modulators demonstrated with free carriers in conventional semiconductors, graphene-based devices have higher carrier mobilities at room temperature with an

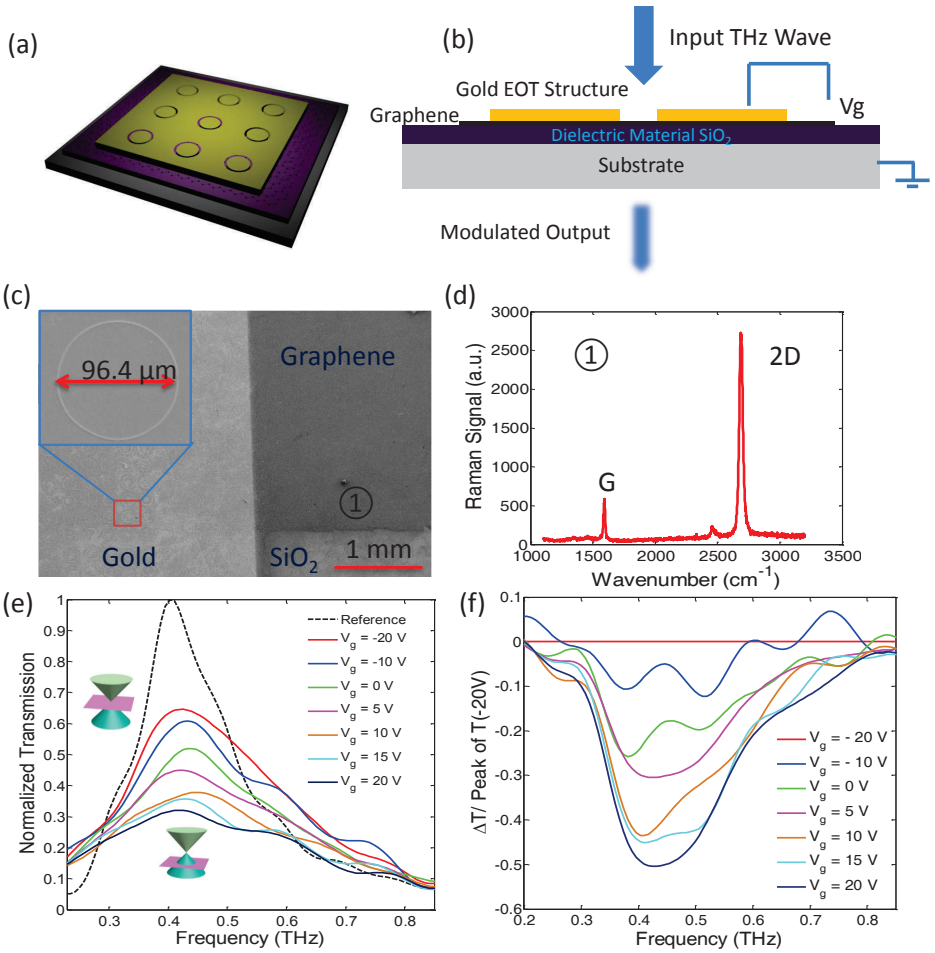

Figure 3. (a) Schematic diagram of the EOT graphene-based THz modulator. (b) The EOT structure is fabricated on graphene, which is placed on a SiO_2/Si substrate. The carrier density of graphene is tuned by applying a gate voltage between the silicon substrate and the EOT structure. (c) SEM image of the fabricated EOT-graphene-based THz modulator. The dark region is graphene underneath. Scale bar is 1 mm. The inset is one element of the EOT ring aperture array. (d) Raman spectrum of graphene underneath the EOT structure. (e) Transmission spectra for the EOT graphene-based THz modulator under different gate voltages between -20 V and +20 V. (f) Transmission difference at different gate voltages, indicating large modulation depth ~50%. Adapted from Ref.[9]

electrically-tunable carrier density. However, the extinction ratio for THz wave modulations obtained with single-layer graphene (SLG) has so far been quite limited because of its small non-resonant intraband absorption in the THz. Recently, many efforts have been devoted to enhance SLG absorption in the THz, including exciting graphene plasmonic resonances,[22] integrating with photonic cavities,[23] and metamaterials.[24] However, no devices demonstrated to date have a combination of a large modulation depth, a high speed, and a designable resonant frequency as shown here.

Here, we use a ring-shaped apertures in a metallic film, i.e., extraordinary optical transmission (EOT) structure, to enhance the intraband absorption in SLG underneath the apertures to form a graphene-based THz modulator with a high extinction ratio [Figs. 3(a) and (b)]. To fabricate this device, the CVD-grown graphene is first transferred onto a SiO_2/Si substrate using standard transfer techniques, followed by electron beam lithography, electron beam evaporation, and lift-off. SEM images of the fabricated device are shown in Fig. 3(c), where the bright region is the gold EOT structure and the dark region is graphene underneath; Raman data is shown in Fig. 3(d), indicating the high-quality of the SLG sample after the transfer. THz transmission spectra of the

device under different bias gate voltages, from −20 V to 20 V, are illustrated in Fig. 3(e), indicating that the peak transmission resonating at ∼0.44 THz changes with the gate voltage. A large modulation depth of ∼50% is observed, as shown in Fig. 3(f), where ΔT is defined as $T(V_g) - T(-20V)$ and normalized to the peak of $T(-20V)$. These results suggest that CMOS-compatible THz modulators with tailored operation frequencies, large on/off ratios, and high speeds can be built.

5. PLASMONIC NATURE OF THE TERAHERTZ CONDUCTIVITY PEAK IN CARBON NANOTUBES

The origin of the pronounced, finite-frequency THz conductivity spectra peak commonly observed in carbon nanotube ensembles remains controversial. Two interpretations have emerged. One is based on the curvature-induced bandgap in non-armchair metallic SWCNTs, while the other is the plasmon resonance in metallic and doped semiconducting SWCNTs. If the hypothesis of curvature-induced bandgaps is correct, the THz peak should (1) happen only in non-armchair metallic SWCNTs, (2) sensitively depend on the diameter, (3) be suppressed by optical pumping or carrier doping, (4) have a strong temperature dependence, and (5) show polarization dependence. If the second hypothesis for the THz peak is correct, (1) It should be detected in both doped semiconducting and metallic SWCNTs; (2) The peak frequency should depend on the nanotube length in a predicted way; (3) The peak intensity should be enhanced by increasing carrier density in semiconducting SWCNTs; (4) Temperature dependence is expected to be weak; and (5) No resonance is expected when the THz polarization is perpendicular to the nanotube direction.

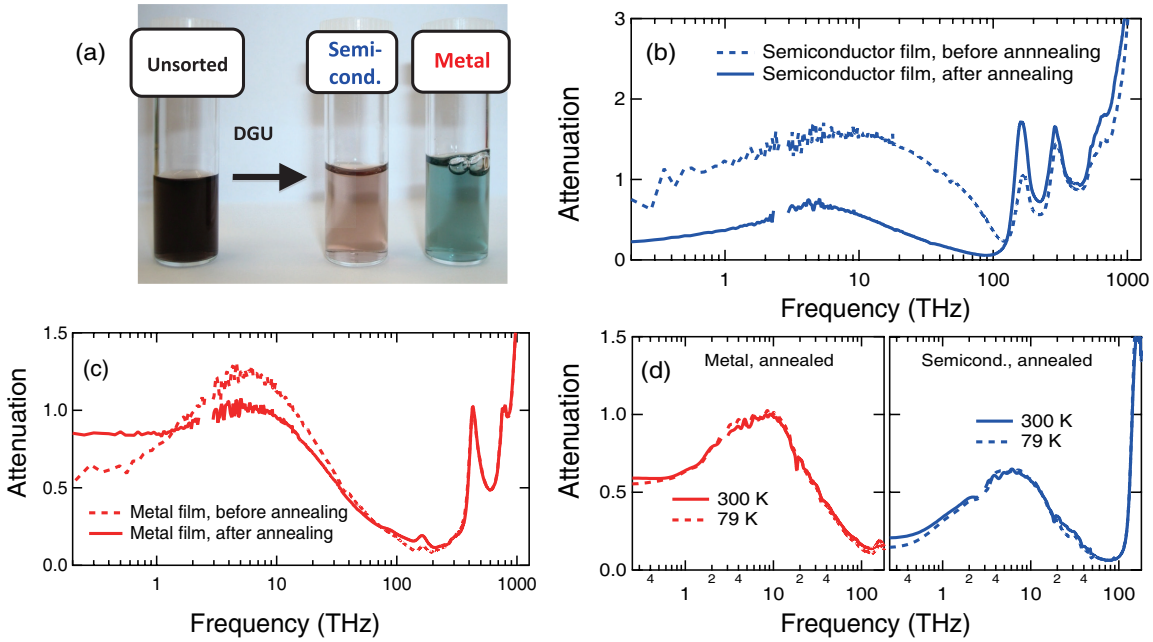

Figure 4. (a) Unsorted, metal-enriched, and semiconductor-enriched SWCNTs suspended in aqueous solution separated via density gradient ultracentrifugation. (b) Semiconductor-enriched SWCNT film before (dashed) and after (solid) annealing. (c) Metal-enriched SWCNT film before (dashed) and after (solid) annealing. (d) Temperature dependence of the THz peak in **[LEFT]** metal-enriched SWCNT film after annealing and **[RIGHT]** semiconductor-enriched SWCNT film before annealing. Adapted from Ref.[11]

Here, we use type-sorted SWCNTs prepared by density gradient ultracentrifugation (DGU)[25–30] to clearly reveal the plasmonic nature of the THz conductivity peak in SWCNTs. Attenuation spectra of semiconductor- and metal-enriched films taken from THz to UV at room temperature both show a broad THz peak [Figs. 4(b) and (c)]. Upon annealing the THz peak is greatly suppressed in semiconductor-enriched films while in metal-enriched films it exhibits only a small decrease. Furthermore, as shown in Fig. 4(d), the attenuation has little dependence on temperature. Based on these observations, the curvature-induced hypothesis can be ruled out, and we can conclude that the THz peak comes from the plasmon resonance of SWCNTs.

6. COLLECTIVE ANTENNA EFFECTS IN HIGHLY ALIGNED CARBON NANAOTUBE ARRAYS

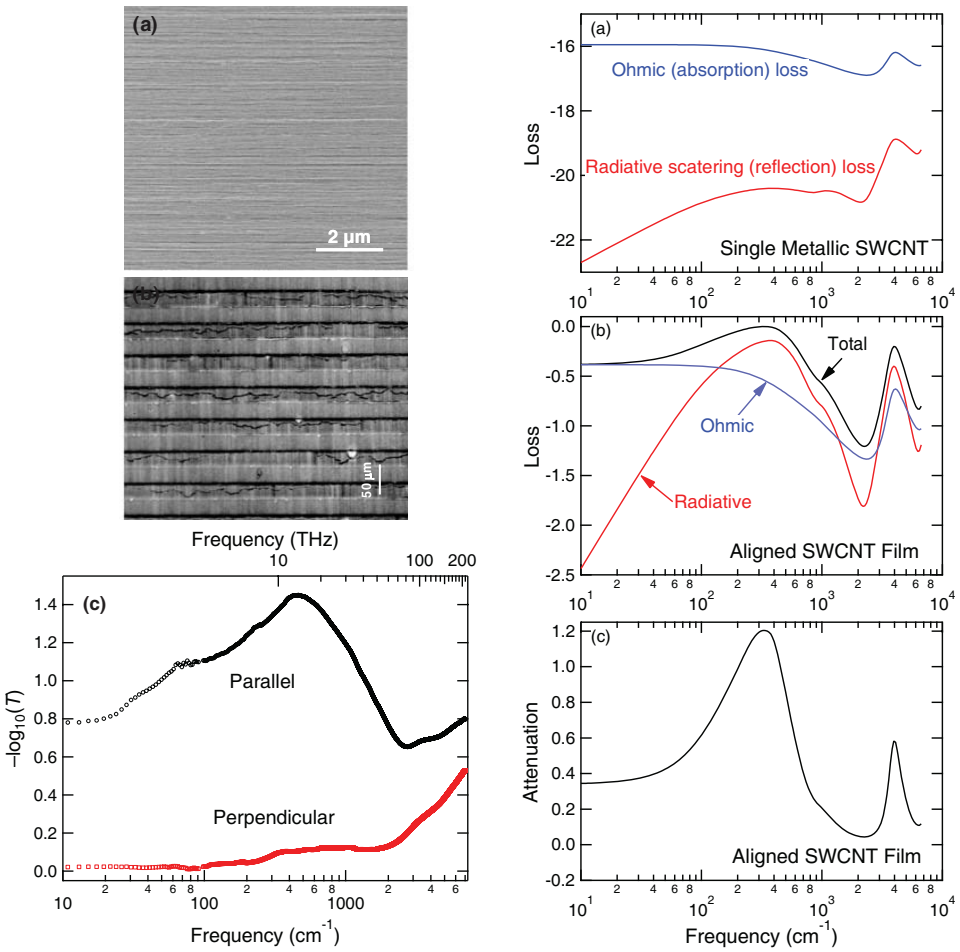

Figure 5. [**LEFT**](a) SEM image of a SWCNT film on a sapphire substrate showing the high degree of nanotube alignment. (b) Optical microscope image of the SWCNT film showing the high uniformity of the nanotube length. (c) THz and infrared attenuation spectra for a highly aligned SWCNT array for polarization parallel (black) and perpendicular (red) to the nanotube alignment direction. [**RIGHT**] The logarithm of absorptive (top trace) and radiative (bottom trace) loss spectra calculated for a single metallic SWCNT with a diameter of 2.7 nm and a length of 75 μm. (b) The logarithm of radiative (red line), Ohmic (blue line), and total (black line) losses calculated for the aligned films consisting of 5×10^4 identical nanotubes with the collective antenna effect. (c) Total normalized attenuation of the film, calculated from the total losses shown in (b). Adapted from Ref.[10]

Recently, films of ultralong and extremely well-aligned SWCNTs have been demonstrated to behave as nearly perfect polarizers in the THz range.[31,32] Such films can be fabricated by CVD growth and dry contact transfer printing processes.[33] Figure 5[LEFT](a) and (b), respectively, show SEM and optical images of an aligned SWCNT film on a sapphire substrate, indicating the high degree of alignment and high uniformity of nanotube lengths ($\sim$75 μm). As shown in Fig. 5[LEFT](c), extreme polarization anisotropy is observed. In the low-frequency THz region ($<$100 cm^{-1}) there is no obvious attenuation when the THz polarization is perpendicular to the nanotubes while strong attenuation exists for the parallel case. With increasing frequency, both the perpendicular and parallel attenuation increases, exhibiting a pronounced and broad peak at $\sim$450 cm^{-1}.

Attenuation comes both from the radiation loss (reflection) and Ohmic loss (absorption).[10] The scattered (or radiated) power as well as the absorbed power for an individual SWCNT can be calculated from the induced

current, $I(z,\omega)$, on the nanotube via the incident electromagnetic wave as

$$P_r(L,\omega) = \frac{\omega^2}{4\epsilon_0 c^3}\int_0^{\pi} d\theta \sin^3\theta \left| \int_{-L/2}^{L/2} I(z,\omega) dz \right|^2, \quad (6)$$

whereas the absorbed power is[34]

$$P_o(L,\omega) = \frac{1}{4\pi R} Re(\sigma_c^{-1}(\omega)) \int_{-L/2}^{L/2} |I(z,\omega)|^2 dz, \quad (7)$$

where L is the length of the nanotube with the origin at the geometric center of the nanotube and $\sigma_c(\omega)$ is the surface conductivity of a metallic SWCNT. The total attenuation is the sum of P_o and P_r. A film consisting of many nanotubes excited within the coherence area of the incident light beam will radiate coherently, and the absorbed power is proportional to the number of excited nanotubes, N, while the scatted power is proportional to N^2. The calculated loss spectra of a single metallic SWCNT and aligned films are presented in Fig. 5[RIGHT](a) and (b), respectively, indicating an important contribution of absorption at the longest wavelengths and a significant contribution of radiative loss in the MIR range, which reflects the collective antenna properties of these aligned, ultralong SWCNTs. The calculated absorption spectrum in Fig. 5[RIGHT](c) reproduces the observed spectra well.

7. ULTRAFAST GENERATION AND DETECTION OF COHERENT PHONONS IN CARBON NANOTUBES

Optical phonons often strong couple with electrons and are behind virtually all energy and phase relaxation processes for electrons in solids. Recently, much attention has been paid to non-perturbatively strong electron-optical-phonon coupling in SWCNTs, which is believed to be responsible for current saturation behaviors in high-field electronic transport as well as for the appearance of a broad and red-shifted Raman feature. In both cases, dynamical quantities of phonons such as lifetimes and dephasing times are the key parameters that characterize the processes. While an extensive literature exists on CW Raman studies, time-domain vibrational measurements directly probing lattice dynamics in SWCNTs have only recently begun.[14,15,35–39] Exactly how optical phonons decay in energy and phase in SWNTs is still an open question. We have carried out a series of coherent phonon spectroscopy studies of SWCNTs[12–15] using spectrally-resolved and temperature-dependent ultrafast pump-probe spectroscopy. A pump pulse initiates coherent lattice vibrations, and then a delayed, spectrally broad probe pulse is incident on the sample, where it induces additional lattice vibrations through impulsive stimulated Raman scattering. The probe photon-energy dependence of phonon amplitude can be well explained within our model.[40,41] Furthermore, the temperature dependence of the observed dephasing rate (not shown in this article) clearly exhibits a thermally-activated component, indicating the presence of the 'exchange-modulation' mechanism.[42] Namely, the high-energy phonon mode dephases via anharmonicity-induced coupling with a lower-frequency mode. Our quantitative analysis provides evidence that the lower-frequency mode responsible for the decay of optical phonons is the RBM.

Figure 6 [LEFT] (a) shows time-domain transmission modulations for a probe at 1.48 eV (840 nm), obtained after subtracting an exponentially decaying electronic component. The oscillatory signal consists of high-frequency and low-frequency contributions. As is confirmed in the Fourier transform in Fig. 6 [LEFT] (b), the low-frequency signal at ∼7 THz corresponds to the RBM, the high-frequency signal is due to the G-mode phonons having a frequency of 47.69 THz (1590.8 cm^{-1}). The detection mechanism of the coherent RBM phonons is through absorption coefficient oscillations as a result of diameter-dependent bandgap.[14,15,40] While the G-phonons can also modify optical constants of SWCNTs, according to theoretical calculations,[40,41] absorption coefficient modulations are expected to be much smaller than those by the RBM.

The G-phonons show drastic changes with the probe wavelength both in amplitude and phase, as shown in Fig. 6 [RIGHT] (a). Figure 6 [RIGHT] (b) shows the optical phonon amplitude as a function of probe energy. The amplitude curve features two peaks with each maximum occurring near the probe energy of 1.46 eV (850 nm) and 1.65 eV (750 nm), respectively, which are separated from each other by the optical phonon energy, while

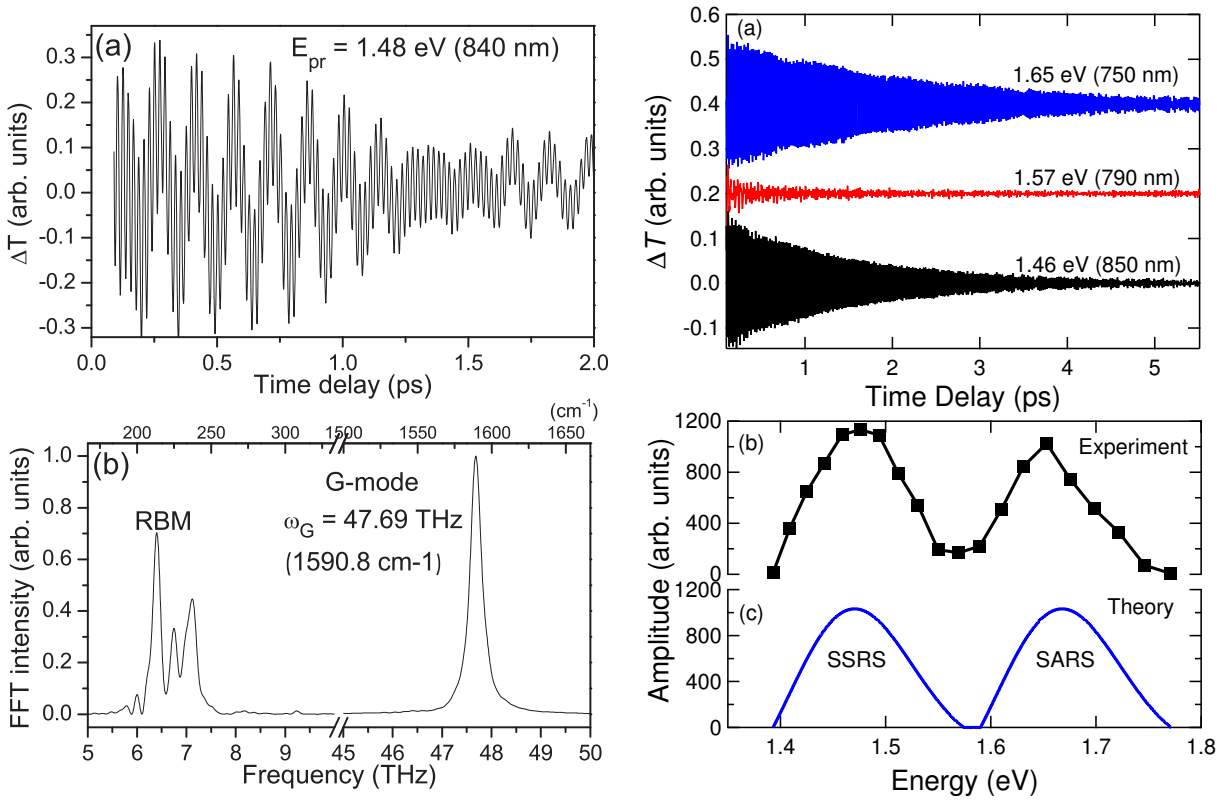

Figure 6. **[LEFT]** (a) Coherent phonon oscillations in SWCNTs, extracted from the pump-probe signal for pump and probe energies of 1.55 eV (800 nm) and 1.48 eV (840 nm), respectively. (b) Corresponding Fourier-transformed spectrum showing radial-breathing modes (RBMs) at 6.0-7.5 THz (200-250 cm^{-1}) and optical phonons (G-mode) at 47.69 THz (1590.8 cm^{-1}). **[RIGHT]** (a) Coherent G-phonon dynamics measured at probe energies of 1.65 eV (750 nm), 1.57 eV (790 nm), and 1.46 eV (850 nm). (b) Coherent phonon amplitude vs. probe energy, exhibiting two peaks at 1.47 eV and 1.66 eV. (c) Simulated spectral intensity for a Gaussian laser spectrum centered at 1.55 eV (800 nm) with a spectral width of 195 meV FWHM. Adapted from Ref.[12]

having a local minimum near the center energy of the laser spectrum. This behavior can be explained by taking into account impulsive stimulated Stokes and anti-Stokes Raman scattering processes. Simulations of the scattering intensity for the two scattering processes were performed assuming a Gaussian laser spectrum centered at 1.55 eV (800 nm) with a spectral width of 195 meV FWHM. The results [Fig. 6 [RIGHT] (c)] show that the signal intensity will be strong on the lower (higher) energy side of the center of the laser spectrum with a peak 100 meV below (above) the center, consistent with the experiment.

ACKNOWLEDGMENTS

This work was supported by the Department of Energy (through Grant No. DE-FG02-06ER46308), the National Science Foundation (through Grants No. OISE-0968405), and the Robert A. Welch Foundation (through Grant No. C-1509). Some of the work presented in this article was performed in collaboration with P. M. Ajayan, A. A. Belyanin, L. G. Booshehri, E. H. Hároz, R. H. Hauge, T. Joo, I. Kawayama, Y.-S. Lim, D. M. Mittleman, A. R. T. Nugraha, R. Saito, G. D. Sanders, C. J. Stanton, M. Tonouchi, J. M. Tour, R. Vajtai, Q. Xu, and K.-J. Yee. Some of the graphene samples were provided by J. P. Frantz at Graphene Platform, Inc.

REFERENCES

[1] Avouris, P., Chen, Z., and Perebeinos, V., "Carbon-based electronics," *Nat. Nanotech.* **2**, 605–615 (2007).

[2] Avouris, P., Freitag, M., and Perebeinos, V., "Carbon-nanotube photonics and optoelectronics," *Nat. Photon.* **2**, 341–350 (2008).

[3] Bonaccorso, F., Sun, Z., Hasan, T., and Ferrari, A. C., "Graphene photonics and optoelectronics," *Nat. Photon.* **4**, 611–622 (2010).

[4] Nanot, S., Hároz, E. H., Kim, J.-H., Hauge, R. H., and Kono, J., "Optoelectronic properties of single-wall carbon nanotubes," *Adv. Mater.* **24**, 4977–4994 (2012).

[5] Hartmann, R. R., Kono, J., and Portnoi, M. E., "Terahertz science and technology of carbon nanomaterials," *arXiv:1311.6035* (2013).

[6] Kono, J., "Ultrafast and nonlinear optics in carbon nanomaterials," *J. Phys.: Condens. Matter* **25**, 050301 (2013).

[7] Ren, L., Zhang, Q., Yao, J., Sun, Z., Kaneko, R., Yan, Z., Nanot, S., Jin, Z., Kawayama, I., Tonouchi, M., Tour, J. M., and Kono, J., "Terahertz and infrared spectroscopy of gated large-area graphene," *Nano Lett.* **12**, 3711–3715 (2012).

[8] Gao, W., Shi, G., Jin, Z., Zhang, Q., Ajayan, P. M., Kono, J., and Xu, Q., "Excitation and active control of propagating surface plasmon polaritons in graphene," *Nano Lett.* **13**, 3698–3702 (2013).

[9] Gao, W., Shu, J., Reichel, K., Nickel, D., He, X., Shi, G., Vajtai, R., Ajayan, P. M., Kono, J., Mittleman, D. M., and Xu, Q., "High-contrast terahertz wave modulation by gated graphene enhanced by extraordinary transmission through ring apertures," *Nano Lett.* **under review** (2013).

[10] Ren, L., Zhang, Q., Pint, C. L., Wójcik, A. K., Bunney, M., Arikawa, T., Kawayama, I., Tonouchi, M., Hauge, R. H., Belyanin, A. A., and Kono, J., "Collective antenna effects in the terahertz and infrared response of highly aligned carbon nanotube arrays," *Phys. Rev. B* **87**, 161401(R) (2013).

[11] Zhang, Q., Hároz, E. H., Jin, Z., Ren, L., Wang, X., Arvidson, R. S., Lüttge, A., and Kono, J., "Plasmonic nature of the terahertz conductivity peak in single-wall carbon nanotubes," *Nano Lett.* **13**, 5991–5996 (2013).

[12] Kim, J.-H., Yee, K.-J., Lim, Y.-S., Booshehri, L. G., Hároz, E. H., and Kono, J., "Dephasing of g-band phonons in single-wall carbon nanotubes probed via impulsive stimulated raman scattering," *Phys. Rev. B* **86**, 161415(R) (2012).

[13] Kim, J.-H., Nugraha, A. R. T., Booshehri, L. G., Hároz, E. H., Sato, K., Sanders, G. D., Yee, K.-J., Lim, Y.-S., Stanton, C. J., Saito, R., and Kono, J., "Coherent phonons in carbon nanotubes and graphene," *Chem. Phys.* **413**, 55–80 (2013).

[14] Lim, Y.-S., Yee, K.-J., Kim, J.-H., Shaver, J., Hároz, E. H., Kono, J., Doorn, S. K., Hauge, R. H., and Smalley, R. E., "Coherent lattice vibrations in carbon nanotubes," *Nano Lett.* **6**, 2696–2700 (2006).

[15] Kim, J.-H., Han, K.-J., Kim, N.-J., Yee, K.-J., Lim, Y.-S., Sanders, G. D., Stanton, C. J., Booshehri, L. G., Hároz, E. H., and Kono, J., "Chirality-selective excitations of coherent phonons in carbon nanotubes by femtosecond optical pulses," *Phys. Rev. Lett.* **102**, 037402 (2009).

[16] Mikhailov, S. A., "Non-linear graphene optics for terahertz applications," *Microelectron. J.* **40**, 712–715 (2009).

[17] Li, Z. Q., Henriksen, E. A., Jiang, Z., Hao, Z., Martin, M. C., Kim, P., Stormer, H. L., and Basov, D. N., "Dirac charge dynamics in graphene by infrared spectroscopy," *Nat. Phys.* **4**, 532–535 (2008).

[18] Horng, J., Chen, C.-F., Geng, B., Girit, C., Zhang, Y., Hao, Z., Bechtel, H. A., Martin, M., Zettl, A., Crommie, M. F., Shen, Y. R., and Wang, F., "Drude conductivity of Dirac fermions in graphene," *Phys. Rev. B* **83**, 165113 (2011).

[19] Wang, F., Zhang, Y., Tian, C., Girit, C., Zettl, A., Crommie, M., and Shen, Y. R., "Gate-variable optical transitions in graphene," *Science* **320**, 206–209 (2008).

[20] Gao, W., Shu, J., Qiu, C., and Xu, Q., "Excitation of plasmonic waves in graphene by guided-mode resonances," *ACS Nano* **6**, 7806–7813 (2012).

[21] Jablan, M., Buljan, H., and Soljačić, M., "Plasmonics in graphene at infrared frequencies," *Phys. Rev. B* **80**, 245435 (2009).

[22] Ju, L., Geng, B., Horng, J., Girit, C., Martin, M., Hao, Z., Bechtel, H. A., Liang, X., Zettl, A., Shen, Y. R., and Wang, F., "Graphene plasmonics for tunable terahertz metamaterials," *Nat. Nano.* **6**, 630–634 (2011).

[23] Seo, M.-A., Park, H.-R., Koo, S.-M., Park, D.-J., Kang, J.-H., Suwal, O.-K., Choi, S.-S., Planken, P. C. M., Park, G.-S., Park, N.-K., Park, Q.-H., and Kim, D.-S., "Terahertz field enhancement by a metallic nano slit operating beyond the skin-depth limit," *Nat. Photon.* **3**, 152–156 (2009).
[24] Lee, S. H., Choi, M., Kim, T.-T., Lee, S., Liu, M., Yin, X., Choi, H. K., Lee, S. S., Choi, C.-G., Choi, S.-Y., Zhang, X., and Min, B., "Switching terahertz waves with gate-controlled active graphene metamaterials," *Nat. Mater.* **11**, 936–941 (2012).
[25] Arnold, M. S., Stupp, S. I., and Hersam, M. C., "Enrichment of single-walled carbon nanotubes by diameter in density gradients," *Nano Lett.* **5**, 713–718 (2005).
[26] Arnold, M. S., Green, A. A., Hulvat, J. F., Stupp, S. I., and Hersam, M. C., "Sorting carbon nanotubes by electronic structure using density differentiation," *Nat. Nanotechnol.* **1**, 60–65 (2006).
[27] Yanagi, K., Miyata, Y., and Kataura, H., "Optical and conductive characteristics of metallic single-wall carbon nanotubes with three basic colors; cyan, magenta, and yellow," *Appl. Phys. Exp.* **1**, 034003 (2008).
[28] Hároz, E. H., Rice, W. D., Lu, B. Y., Ghosh, S., Hauge, R. H., Weisman, R. B., Doorn, S. K., and Kono, J., "Enrichment of armchair carbon nanotubes via density gradient ultracentrifugation: Raman spectroscopy evidence," *ACS Nano* **4**, 1955–1962 (2010).
[29] Hároz, E. H., Duque, J. G., Lu, B. Y., Nikolaev, P., Arepalli, S., Hauge, R. H., Doorn, S. K., and Kono, J., "Unique origin of colors of armchair carbon nanotubes," *J. Am. Chem. Soc.* **134**, 4461–4464 (2012).
[30] Hároz, E. H., Duque, J. G., Tu, X., Zheng, M., Walker, A. R. H., Hauge, R. H., Doorn, S. K., and Kono, J., "Fundamental optical processes in armchair carbon nanotubes," *Nanoscale* **5**, 1411–1439 (2013).
[31] Ren, L., Pint, C. L., Booshehri, L. G., Rice, W. D., Wang, X., Hilton, D. J., Takeya, K., Kawayama, I., Tonouchi, M., Hauge, R. H., and Kono, J., "Carbon nanotube terahertz polarizer," *Nano Lett.* **9**, 2610–2613 (2009).
[32] Ren, L., Pint, C. L., Arikawa, T., Takeya, K., Kawayama, I., Tonouchi, M., Hauge, R. H., and Kono, J., "Broadband terahertz polarizers with ideal performance based on aligned carbon nanotube stacks," *Nano Lett.* **12**, 787–790 (2012).
[33] Pint, C. L., Xu, Y.-Q., Moghazy, S., Cherukuri, T., Alvarez, N. T., Hároz, E. H., Mahzooni, S., Doorn, S. K., Kono, J., Pasquali, M., and Hauge, R. H., "Dry contact transfer printing of aligned carbon nanotube patterns and characterization of their optical properties for diameter distribution and alignment," *ACS Nano* **4**, 1131–1145 (2010).
[34] Wu, T. and King, R., "The cylindrical antenna with nonreflecting resistive loading," *IEEE Trans. Antennas Propag.* **13**, 369–373 (1965).
[35] Gambetta, A., Manzoni, C., Menna, E., Meneghetti, M., Cerullo, G., Lanzani, G., Tretiak, S., Piryatinski, A., Saxena, A., Martin, R. L., and Bishop, A. R., "Real-time observation of nonlinear coherent phonon dynamics in single-walled carbon nanotubes," *Nat. Phys.* **2**, 515–520 (2006).
[36] Kato, K., Ishioka, K., Kitajima, M., Tang, J., Saito, R., and Petek, H., "Coherent phonon anisotropy in aligned single-walled carbon nanotubes," *Nano Lett.* **8**, 3102–3108 (2008).
[37] Song, D., Wang, F., Dukovic, G., Zheng, M., Semke, E. D., Brus, L. E., and Heinz, T. F., "Direct measurement of the lifetime of optical phonons in single-walled carbon nanotubes," *Phys. Rev. Lett.* **100**, 225503 (2008).
[38] Lüer, L., Gadermaier, C., Crochet, J., Hertel, T., Brida, D., and Lanzani, G., "Coherent phonon dynamics in semiconducting carbon nanotubes: A quantitative study of electron-phonon coupling," *Phys. Rev. Lett.* **102**, 127401 (2009).
[39] Lee, Y. J., Parekh, S. H., Fagan, J. A., and Cicerone, M. T., "Phonon dephasing and population decay dynamics of the g-band of semiconducting single-wall carbon nanotubes," *Phys. Rev. B* **82**, 165432 (2010).
[40] Sanders, G. D., Stanton, C. J., Kim, J.-H., Yee, K.-J., Lim, Y.-S., Hároz, E. H., Booshehri, L. G., Kono, J., and Saito, R., "Resonant coherent phonon spectroscopy of single-walled carbon nanotubes," *Phys. Rev. B* **79**, 205434 (2009).
[41] Sanders, G. D., Nugraha, A. R. T., Sato, K., Kim, J.-H., Kono, J., Saito, R., and Stanton, C. J., "Theory of coherent phonons in carbon nanotubes and graphene nanoribbons," *J. Phys.: Condens. Matter* **25**, 144201 (2013).
[42] Harris, C. B., Shelby, R. M., and Cornelius, P. A., "Effects of energy exchange on vibrational dephasing times in raman scattering," *Phys. Rev. Lett.* **38**, 1415–1419 (1977).